Analytical and Experimental Investigations on Mitigation of Interference in a DBF MIMO Radar

Jonathan Bechter, *Graduate Student Member, IEEE*, Muhammad Rameez, and Christian Waldschmidt, *Senior Member, IEEE*

(Invited Paper)

***Abstract*— As driver assistance systems and autonomous driving are on the rise, radar sensors become a common device for automobiles. The high sensor density leads to the occurrence of interference, which decreases the detection capabilities. Here, digital beamforming (DBF) is applied to mitigate such interference. A DBF system requires a calibration of the different receiving channels. It is shown how this calibration completely changes the DBF beam pattern required to cancel interferences, if the system has no IQ receiver. Afterward, the application of DBF on a multiple-input multiple-output (MIMO) radar is investigated. It is shown that only the real aperture and not the virtual one can be used for interference suppression, leading to wide notches in the pattern. However, for any target the large virtual aperture can be exploited, even if interferers are blinded out. Moreover, the wide notches for interference suppression of the real aperture appear narrow in the virtual aperture for target localization. The results are verified by measurements with time-multiplexing MIMO radar.**

***Index Terms*— Automotive radar, beamforming, multiple-input multiple-output (MIMO), radar receivers, radar systems, signal processing.**

I. INTRODUCTION

FOR the realization of driver assistance systems and autonomous driving, automobiles get equipped with various sensors. For higher robustness, a mixture of different sensor types, like camera, radar, or ultrasonic, is desired. Thus, the amount of radar sensors used in daily traffic will increase in the future. Likewise, interferences between those sensors will occur more often. In the scenario in Fig. 1, the side radar of a truck interferes with the front sensor of a passing car. Interference can occur even if the truck is not in the field of view of the car's sensor. Automotive radars usually transmit frequency ramps with frequency modulated continuous wave (FMCW) or chirp sequence modulations. Interferences occur most likely as depicted in Fig. 2(a), where the frequency ramps transmitted by truck and car have different slopes and intersect [1]. As long as the truck's signal passes the receiver bandwidth of the car's sensor (dashed lines), interference occurs. Such interferences increase the noise level and reduce the probability to detect radar targets [2]. It is also possible that both sensors transmit frequency ramps with identical slopes [see Fig. 2(b)]. In this case, interference can result in a ghost target, but it is very unlikely that such ramps fall into each other's receiver bandwidths [1], [3].

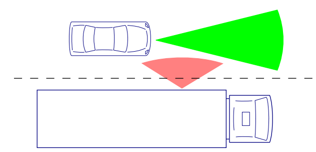

Fig. 1. Typical highway scenario: a car passes a truck. The side sensor of the truck may cause interference in the car's front sensor. The fields of view are indicated in red and green.

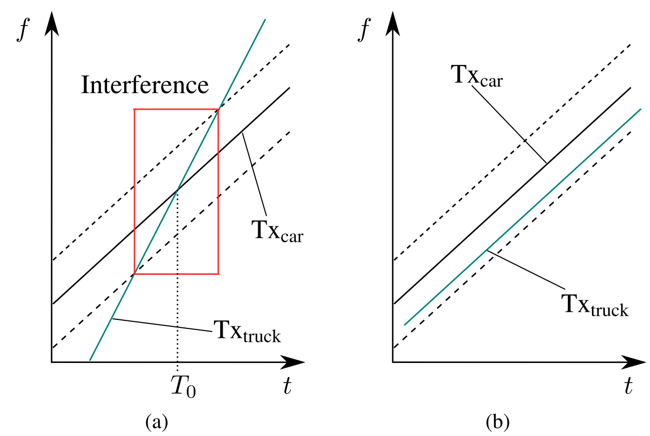

Fig. 2. Frequency ramps transmitted by the sensors of the vehicles in Fig. 1 can interfere in different ways. (a) Receiver bandwidth of the car's sensor limits the interference duration (dashed lines). (b) Parallel ramp generates a ghost target only if it falls within the receiver bandwidth.

There are multiple methods to counteract interferences in multiple-input multiple-output (MIMO) radars. In military applications, the spatial diversity provided by statistical MIMO radars can be used for jamming suppression [4]. For collocated MIMO radars, which are under investigation here, digital beamforming (DBF) algorithms for the suppression of intentional jamming were derived in [5]. They show good simulation results with an MIMO radar with ten transmit and ten receive elements. Investigations on adaptive DBF for automotive single-input multiple-output (SIMO) radar were

Manuscript received October 14, 2016; revised January 31, 2017; accepted February 5, 2017. Date of publication February 24, 2017; date of current version May 4, 2017.

J. Bechter and C. Waldschmidt are with the Institute of Microwave Engineering, Ulm University, 89081 Ulm, Germany (e-mail: jonathan.bechter@uni-ulm.de; christian.waldschmidt@uni-ulm.de).

M. Rameez was with the Institute of Microwave Engineering, Ulm University, 89081 Ulm, Germany. He is now with the Department of Mathematics and Natural Sciences, Blekinge Institute of Technolgy, 37141 Karlshamn, Sweden (e-mail: muhammad.rameez@bth.se).

Color versions of one or more of the figures in this paper are available online at http://ieeexplore.ieee.org.

Digital Object Identifier 10.1109/TMTT.2017.2668404

shown in [6], supported by simulation data. Instead of using adaptive algorithms, DBF can be realized with beam and notch steering. Such algorithms place minima and maxima at chosen angles in the beam pattern and require knowledge of at least the direction of arrival (DoA) of the interference. One way to find this DoA is an estimation using the interfered samples of the time signal as shown in [7]. In [8], we investigated notch steering for an SIMO radar. It turned out that for systems without IQ receiver, interference cannot be canceled by steering a notch toward its direction alone. The interference energy is split onto multiple DoAs.

As the chirp sequence radar does not require an IQ receiver, this issue is further pursued here. As a new contribution of this paper, analytical equations are derived in Section II, which describe the DoAs affected by interference energy. It is shown that certain design parameters take severe influence hereon.

Future automotive radar sensors will most likely be realized as MIMO systems. Therefore, Section III addresses the application of an MIMO radar system for interference mitigation with DBF. Orthogonal transmit signals for an MIMO radar are typically realized by time, frequency, or code multiplexing. This ends up in a large virtual aperture, which improves angular resolution.

It is shown that an interfering signal does not obey the virtual aperture. Thus, when beamforming is applied on the virtual array, it affects interferences only with the real aperture size, leading to wider notches for interference cancellation. At the same time, desired signals are affected by the larger virtual aperture, and therefore they experience more narrow notches. When an interfering signal transmitted by a car is suppressed with a notch, the desired signals reflected from the car are also affected. However, those desired signals experience narrower notches because of the large virtual MIMO aperture. This reduces the undesired effect of masking targets which are located in close proximity to interferers.

In Section IV, the application of a null steering digital beamformer to mitigate interference in a 77-GHz time-division multiplexing (TDM) MIMO radar with two transmit and four receive antennas is shown. The problems derived earlier in this paper are taken into account to clearly suppress the interference.

This paper notation handles matrices with bold capital letters. Frequency signals are written in capital letters, while time signals and matrix entries are written in small letters.

II. Interference in a DBF Radar Without IQ Mixer

Application of DBF requires a system with multiple independently sampled channels, like the receiver shown in Fig. 3. N antennas are connected to an Rx (receiver) chip with transmission lines of lengths l_i. The signals are down converted, filtered, and further processed in the chip. After the signals are digitized and Fourier transformed, DBF is applied. Its basic principle is based on the phase difference

$$\Delta\varphi = kd \sin\vartheta \tag{1}$$

between two channels with element spacing d, for a signal with free-space wavenumber k and incident angle ϑ. The beamformer uses weights w_n to combine the data $S_n(f)$ of each channel to the DBF output

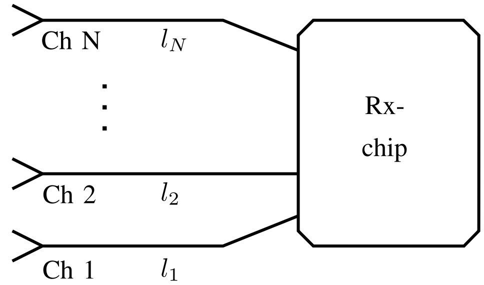

Fig. 3. Radar receiver with N independent Rx channels. The antennas are connected to an Rx-chip with transmission lines of lengths l_n for down conversion and further processing.

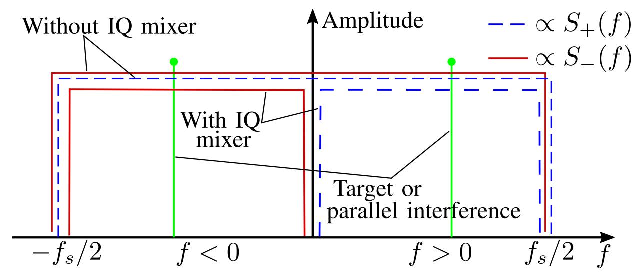

Fig. 4. Baseband spectrum is limited by the sampling frequency f_s. Without IQ mixer, the interference $S_+(f)$ for $t > 0$ affects identical frequencies as $S_-(f)$ for $t < 0$.

$$S_{\mathrm{DBF}}(f) = \sum_{n=1}^{N} w_n S_n(f). \tag{2}$$

By choosing appropriate weights, undesired signals can be suppressed and desired signals amplified, depending on their DoA. This way, interference from the truck in Fig. 1 can be mitigated by suppressing the DoA of its sensor. However, if the car's receiver does not provide an IQ mixer, additional requirements must be met for interference suppression, which are reviewed from [8] for an ideal system. Afterward, it is derived how the effect changes in real systems because of the line lengths l_n in Fig. 3.

A. Image Frequency Problem in an Ideal System

In an ideal system, it is assumed that all transmission lines in Fig. 3 have the same length, so that the phase differences between the channels obey (1). After down conversion, the interference signal behaves like a frequency ramp [9]. In time domain, it can be described as

$$s_{\mathrm{int}}(t) \propto \cos(a(t - T_0)^2 + b + \Delta\varphi). \tag{3}$$

The abbreviations a and b are described in detail in [9]. They are determined by the frequency difference and the zero phases of the two ramps in Fig. 2(a). T_0 is the point in time when the ramps intersect and the down converted frequency is zero. To simplify the following derivation, T_0 is set to zero. It can be seen from Fig. 2(a) that the part of the down-converted interference signal for $t > 0$ passes through the whole baseband filter, and therefore has frequency components in the whole baseband spectrum. This signal part is called $S_+(f)$ and is indicated with a blue dashed rectangle in Fig. 4.

The same is valid for the interference signal $S_-(f)$ for $t < 0$, shown with the red rectangle. Without IQ mixer, the frequency components $S_+(f)$ and $S_-(f)$ cannot be separated; it is an image frequency problem.

According to (3), the time-domain interference signal is real-valued and an even function for $T_0 = 0$. Thus, we can state that $S_+(f) = S_-^*(f)$. Depending on the sign of a, we get

$$S_+(f > 0) \propto \exp(jkd \sin \vartheta) \tag{4}$$

for positive a, and therefore

$$S_-(f > 0) \propto \exp(-jkd \sin \vartheta) = \exp(jkd \sin(-\vartheta)) \tag{5}$$

or

$$S_+(f > 0) \propto \exp(-jkd \sin \vartheta) \tag{6}$$

for negative a, and therefore

$$S_-(f > 0) \propto \exp(jkd \sin \vartheta). \tag{7}$$

This means, that an interference signal with DoA ϑ also has a component that belongs to the DoA $-\vartheta$. If a beamformer is used to cancel interference, it must take into account both DoAs. It is not sufficient to remove the interference DoA alone [8]. The further derivations are all done for (4) and (5).

For comparison, Fig. 4 also shows the spectrum of a target signal that behaves similar to a parallel interference, as depicted in Fig. 2(b). Such a signal has two complex conjugate frequency components, which are separated into the positive and negative parts of the spectrum. Although they are complex conjugate as $S_+(f)$ and $S_-(f)$, the limitation to one side of the spectrum keeps the angle information unambiguous. Fig. 4 also shows how an IQ receiver changes the spectrum of $S_+(f)$ and $S_-(f)$. In this case, only the real interference DoA affects the desired signal.

B. Image Frequency Problem in a Real System

The image frequency problem is now extended to a real system. In this case, the transmission lines $l_1 \ldots l_N$ in Fig. 3 will not have the same length anymore. A different line length in the RF path leads to a constant time delay for all signals on that channel. This causes an additional phase shift φ_{err} and alters (1) to

$$\Delta\varphi = kd \sin \vartheta + \varphi_{\text{err}}. \tag{8}$$

Such phase shifts can be determined in a calibration measurement and fixed in the signal processing by multiplication with $\exp(-j\varphi_{\text{err}})$. Fig. 5 shows the phase difference between two channels as a function of $\sin \vartheta$. In the ideal system discussed above, this phase difference is a straight line described by (1), while in the real system this line is shifted by φ_{err}. The calibration cancels φ_{err} and results in the same behavior as in the ideal case. This leads to (1) and (4) for target signals and $S_+(f)$. However, this is not the case for $S_-(f)$ in (5). Before the array calibration, it is

$$S_-(f) = S_+^*(f) \propto \exp(-jkd \sin \vartheta - j\varphi_{\text{err}}). \tag{9}$$

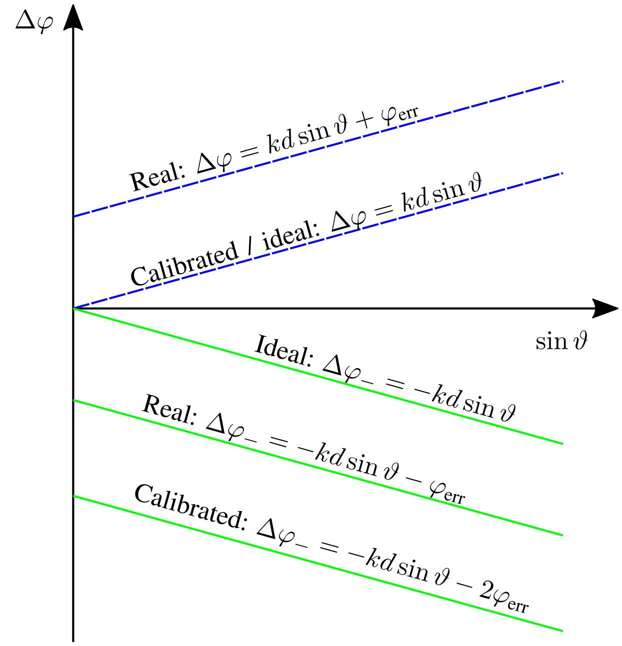

Fig. 5. Comparison of phase differences $\Delta\varphi$ of $S_+(f)$ (blue dashed curves) and $\Delta\varphi_-$ of $S_-(f)$ (green solid curves) between two channels in a real, an ideal, and a calibrated array.

After calibration, (9) changes to

$$\begin{aligned} S_-(f) &\propto \exp(jkd \sin(-\vartheta) - j\varphi_{\text{err}}) \cdot \exp(-j\varphi_{\text{err}}) \\ &= \exp(jkd \sin(-\vartheta) - 2j\varphi_{\text{err}}). \end{aligned} \tag{10}$$

The phase shift has not been removed, but its value changed to $-2\varphi_{\text{err}}$. This is shown in the bottom part of Fig. 5. By calibration, the phase progression is not shifted to the ideal curve, but moved downward instead.

Thus, in order to remove $S_-(f)$ with DBF, it is not reasonable to place a notch at $-\vartheta$ in a real system. Still, this interference energy must be taken into account. Consider the phase difference of $S_-(f)$ between two channels after calibration

$$\Delta\varphi_- = -kd \sin \vartheta - 2\varphi_{\text{err}} \stackrel{!}{=} kd \sin \hat{\vartheta}. \tag{11}$$

This phase difference represents an angle $\hat{\vartheta}$ in the calibrated array

$$\hat{\vartheta} = -\arcsin\left(\sin \vartheta + \frac{2\varphi_{\text{err}}}{kd}\right). \tag{12}$$

As an example, we assume a four-element uniform linear array with element distances of $\lambda/2$ and interference from $\vartheta = -10°$. In an ideal system, the beamformer would have to cancel the DoAs $\pm 10°$. In a real system operating at 76 GHz, a line length difference of 260 μm between the first two channels shifts the interference DoA from 10° to

$$\hat{\vartheta} = -13.1° \tag{13}$$

whereby an effective relative permittivity of 2.3 is assumed. Instead of removing the DoAs $\pm 10°$, the beamformer must cancel $-10°$ and $-13.1°$. Between the third and fourth channel, we assume a line length difference of 650 μm. Through

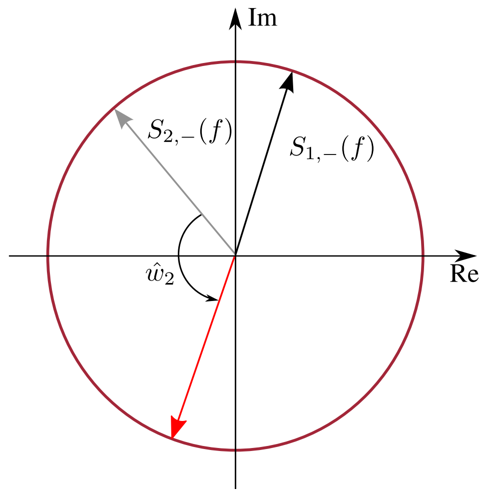

Fig. 6. Phase difference between the interference signal on two channels is determined by the interference DoA. The interference signal $S_{2,-}(f)$ in channel 2 is adjusted with $\hat{w}_2$ and added to $S_{1,-}(f)$ for interference cancellation.

the resulting phase difference, the interference appears to have the DoAs $-10°$ and

$$\hat{\vartheta} = -55.7°. \tag{14}$$

The second DoA differs from (13), what makes the application of classical notch steering algorithms difficult. Steering notches in the beam pattern at $-13.1°$ and $-55.7°$ will not remove these interference components, because they do not obey a classical steering vector.

Instead of using a classical notch steering algorithm, the channels can be combined pairwise to remove the interference in multiple stages. In Fig. 6, the signal component $S_-(f)$ is considered as complex vectors $S_{1,-}(f)$ and $S_{2,-}(f)$ on the first two channels. When the interference DoA is known, the phase difference between the channels is found with (10). With this knowledge, the vector $S_{2,-}$ is rotated through multiplication with the complex value $\hat{w}_2$, resulting in

$$S_{1,-}(f) + \hat{w}_2 S_{2,-}(f) \stackrel{!}{=} 0. \tag{15}$$

The same approach for channels 3 and 4 results in

$$S_{3,-}(f) + \hat{w}_4 S_{4,-}(f) \stackrel{!}{=} 0. \tag{16}$$

Afterward, $S_+(f)$ is removed using $\hat{w}_3$ by

$$(S_{1,+}(f) + \hat{w}_2 S_{2,+}(f)) + \hat{w}_3(S_{3,+}(f) + \hat{w}_4 S_{4,+}(f)) \stackrel{!}{=} 0. \tag{17}$$

This leads to an interference-free signal. Fig. 7 shows the processing scheme extended for a beamformer with an arbitrary amount of channels. The block combining four channels for interference cancellation, which was described in (15)–(17), is repeated multiple times. The outputs are multiplied with additional weights and summed up to steer the beam into desired DoAs. Removing a single interference therefore requires four channels, while this number is doubled for each additional interference to be removed with the beamformer.

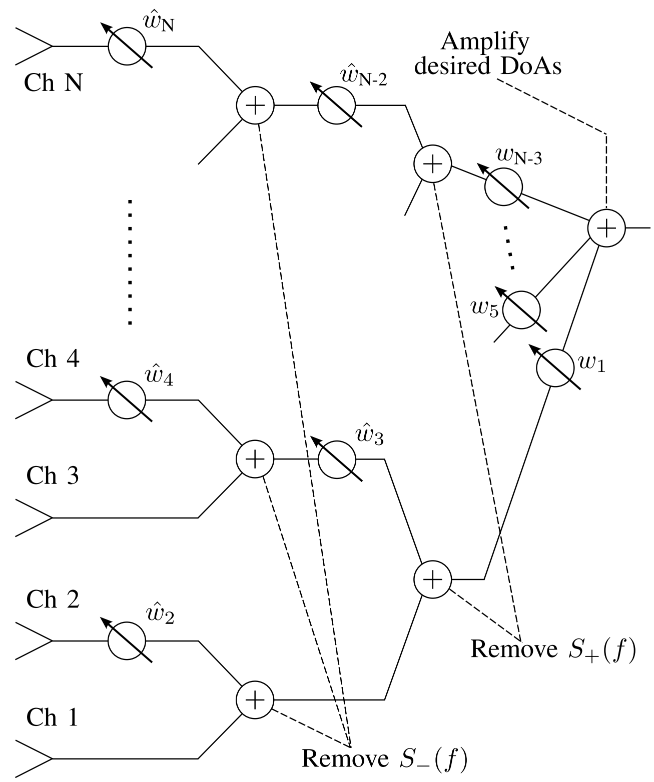

Fig. 7. First step removes the $S_-(f)$ interference component. The second step removes $S_+(f)$. The remaining degrees of freedom steer beams toward desired DoAs.

The weights for the beamformer (2) are given as the product of the factors along the respective paths in Fig. 7, for example,

$$w_2 = \hat{w}_2 \cdot w_1 \tag{18}$$

$$w_3 = \hat{w}_3 \cdot w_1 \tag{19}$$

$$w_4 = \hat{w}_4 \cdot \hat{w}_3 \cdot w_1. \tag{20}$$

III. DBF With an MIMO Radar

The capabilities of a beamformer are typically limited by the overall aperture size and the number of available channels. An MIMO radar uses multiple transmitters and multiple receivers to offer increased aperture size and additional virtual antenna elements with comparably low hardware effort. The transmitted signals must be orthogonal, so that the signal path from each transmitter to each receiver can be distinguished and processed separately. A large aperture and many independent channels are beneficial for DBF. Therefore, the applicability of an MIMO system is investigated here.

Fig. 8 shows a scheme of an MIMO radar with two transmit and two receive elements. The signal paths from the transmitters to the receivers can be described with a channel matrix $\mathbf{H}_{\mathrm{MIMO}}$. According to [10], with the notation used in this paper, the entries of the channel matrix obey

$$\mathrm{h}_{\mathrm{MIMO},m,n} \propto \exp(jk(x_{\mathrm{Tx},m} + x_{\mathrm{Rx},n}) \sin\vartheta) \tag{21}$$

where $x_{\mathrm{Tx},m}$ and $x_{\mathrm{Rx},n}$ describe the physical locations of the transmit and receive elements. $\mathrm{h}_{\mathrm{MIMO},m,n}$ is the channel matrix entry for the signal path from transmitter m to receiver n. For a

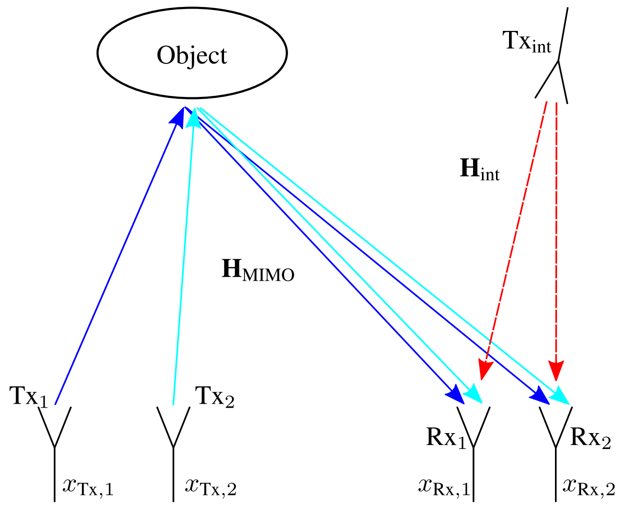

Fig. 8. Matrix $\mathbf{H}_{\mathrm{MIMO}}$ describes the signal paths between the transmitters and the receivers (blue solid lines) under far-field conditions. The interference channel matrix $\mathbf{H}_{\mathrm{int}}$ describes the paths from an interfering sensor $\mathrm{Tx}_{\mathrm{int}}$ to the receivers (red dashed lines), which is independent of $x_{\mathrm{Tx},m}$.

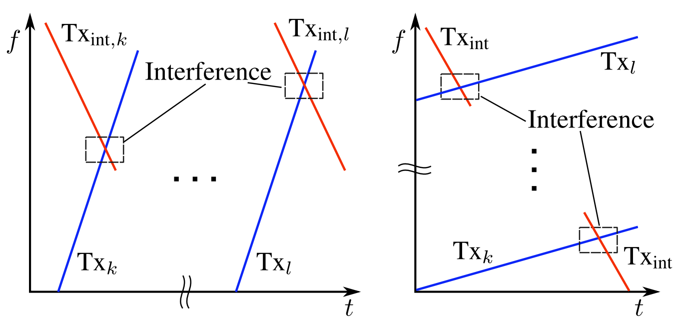

(a) (b)

Fig. 9. Interference in different transmit signals Tx_k and Tx_l for (a) TDM and (b) FDM MIMO radars.

radar with M transmitters and N receivers, the matrix $\mathbf{H}_{\mathrm{MIMO}}$ has $M \cdot N$ entries and describes the phase differences between the elements of the virtual array. Each target in the radar channel generates a phase coherent response in the virtual array. So, based on (21), we can apply DBF.

The channel matrix $\mathbf{H}_{\mathrm{int}}$ in Fig. 8 for interference transmitted by $\mathrm{Tx}_{\mathrm{int}}$ is independent of the locations $x_{\mathrm{Tx},m}$. Thus, interfering signals do not obey (21), and, for interference cancellation with DBF, the wide virtual aperture cannot be used. Similar to (21), the entries of $\mathbf{H}_{\mathrm{int}}$ can be described as

$$\mathrm{h}_{\mathrm{int},m,n} \propto A_m \cdot \exp(jkx_{\mathrm{Rx},m} \sin\vartheta + j\phi_m). \quad (22)$$

The amplitude A_m and phase ϕ_m include a dependence on the transmit channel m. This originates from the orthogonality requirement of the transmit signals and is explained in the following.

Orthogonal transmit signals are realized with TDM, frequency-division multiplexing (FDM), or code-division multiplexing schemes, as described in [11]–[14]. For a TDM MIMO radar, Fig. 9(a) shows frequency ramps transmitted by two different transmitters Tx_k and Tx_l and interference through another sensor's frequency ramps $\mathrm{Tx}_{\mathrm{int},k}$ and $\mathrm{Tx}_{\mathrm{int},l}$. When the ramp repetition rate of both sensors is not identical,

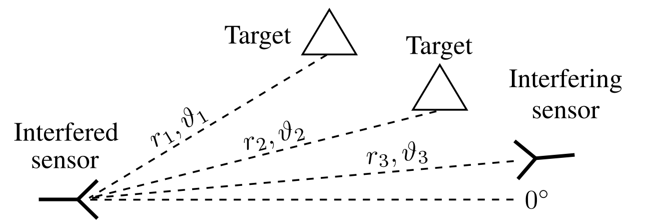

Fig. 10. Positions in the measurement setup are $r_1 = 3.8\,\mathrm{m}$, $\vartheta_1 = 31°$, $r_2 = 5\,\mathrm{m}$, $\vartheta_2 = 14°$, and $r_3 = 6\,\mathrm{m}$, $\vartheta_3 = 5°$.

interference in Tx_k and Tx_l occurs at different frequencies. Additionally, after down conversion, the different zero phases of Tx_k and Tx_l will show up in the baseband interference signal. These effects lead to the phase shift ϕ_m. When interference occurs at different points in time in the frequency ramps, the window function applied in signal processing changes A_m. It is also possible that the interference does not occur in each frequency ramp, leading to $A_m = 0$ for certain m.

Interference in an FDM MIMO radar is also likely to occur at another part of the frequency ramp for different transmitters [see Fig. 9(b)]. This leads to similar effects as in the TDM case. Because of the described phase and amplitude inconsistencies, ϕ_m and A_m, DBF can cancel interference only by steering notches with the signals of single transmitters.

Therefore, the signals summed up to remove $S_+(f)$ and $S_-(f)$ in Fig. 7 in an MIMO array must all belong to the same transmitter. After interferences are canceled this way, beams toward desired DoAs are formed with the virtual array.

IV. Application of DBF on a 2×4 MIMO Radar

The described DBF processing is applied on an MIMO radar with two transmit and four receive channels. It has an eight-element virtual aperture with the element positions

$$d_1 = 0 \quad d_2 = 1.67\lambda \quad d_3 = 3.87\lambda \quad d_4 = 4\lambda$$
$$d_5 = 5.67\lambda \quad d_6 = 6.56\lambda \quad d_7 = 7.87\lambda \quad d_8 = 10.56\lambda.$$

The free-space wavelength λ is 4 mm for the operating frequency of 76 GHz. In a calibration measurement, the phase differences $\Delta\varphi$ between the channels, according to Fig. 5, are determined. The following phases $\varphi_{\mathrm{err},n}$ in radians are found for the channels n:

$$\begin{aligned}
\varphi_{\mathrm{err},1} &= 0 & \varphi_{\mathrm{err},5} &= 3.42\\
\varphi_{\mathrm{err},2} &= 0.96 & \varphi_{\mathrm{err},6} &= 4.39\\
\varphi_{\mathrm{err},3} &= 1.96 & \varphi_{\mathrm{err},7} &= 5.40\\
\varphi_{\mathrm{err},4} &= 1.83 & \varphi_{\mathrm{err},8} &= 5.26.
\end{aligned}$$

The sensor transmits rising frequency ramps with a bandwidth of 600 MHz. The transmit elements are switched with a time delay of 50 μs to realize the TDM MIMO operation. In the measurement setup discussed here, targets are located at the positions ($r_1 = 3.8\,\mathrm{m}$, $\vartheta_1 = 31°$), ($r_2 = 5\,\mathrm{m}$, $\vartheta_2 = 14°$), and ($r_3 = 6\,\mathrm{m}$, $\vartheta_3 = 5°$) (see Fig. 10). The third target is an interfering radar sensor which transmits falling frequency ramps with center frequency 76 GHz and bandwidth 300 MHz with a single transmit antenna. The other two targets are corner reflectors. All objects in the radar channel are static, so that

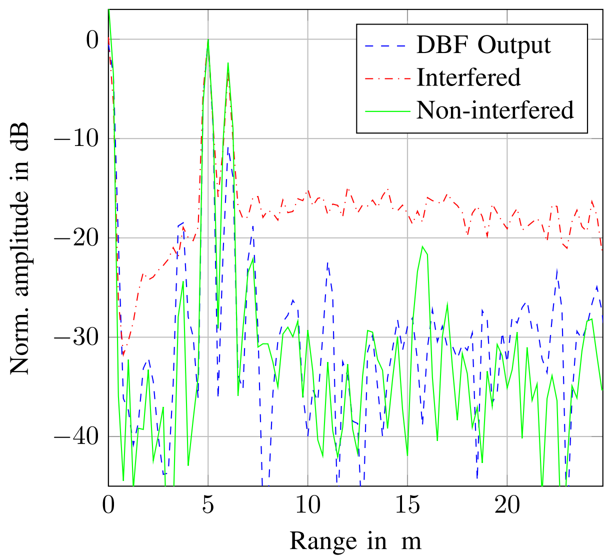

Fig. 11. Measurement of the interfered signal after noncoherent integration, the interference-free signal on a single channel, and the DBF output. The graphs are normalized to the target at 5 m.

the effect of motion induced phase migration in TDM MIMO radars [11], [15] is avoided. This effect would not reduce the performance of steering notches, but without a compensation algorithm it would degrade the beam steering toward desired DoAs.

Fig. 11 shows the spectrum of an interference-free measurement for a single channel and an interfered measurement after a noncoherent integration over the 8 virtual channels. Without interference, the signal-to-noise-and-interference ratio (SNIR) of the first target is 9.6 dB, of the second target 29 dB, and of the third target 26.8 dB. Due to the interference, the overall noise floor is increased. The SNIR values drop to 1, 17.9, and 14.5 dB, respectively. All SNIR values are determined by an ordered statistics constant false alarm rate [16] algorithm.

At first, the coexistence of $S_+(f)$ and $S_-(f)$ is verified. The frequency bins, which correspond to distances above 20 m, are free of target reflections, so there is only the interference signal and noise present. A DoA estimation with the Capon beamformer [17] is applied on those frequency bins to find the interference DoA. Only the signals from the first transmit to all receive elements are evaluated therefore. As shown in the previous section, the DoA estimation of the interference cannot benefit from the virtual MIMO aperture.

In Fig. 12(a), the estimation is shown after the array is calibrated with $\exp(-j\varphi_{\mathrm{err},n})$. The strongest peak occurs at +5°, which is the true interference DoA. Another peak appears at 16°. This result is compared with a simulation. An interference signal, which obeys (3) and (8), is simulated for the same array as used in the measurement. The DoA estimation on the simulation data also shows two strong peaks at 5° and 16°. When the simulation is done with a complex exponential function instead of a cosine in (3), the peak at 16° disappears (not shown in the figure). The complex signal corresponds to using an IQ mixer, and in this case $S_-(f)$ does not exist. Thus, the peak generated at 16° in the measurement is created by $S_-(f)$. This peak is, both in the simulation and

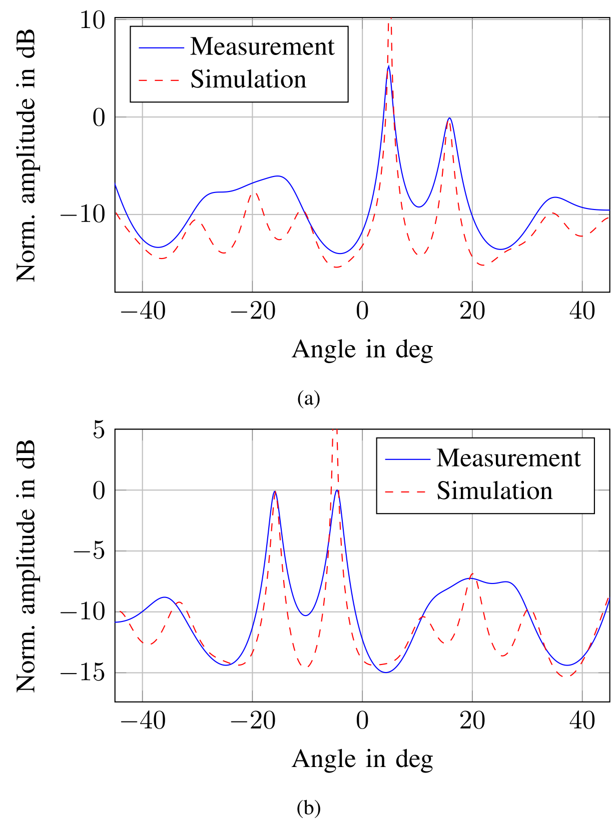

Fig. 12. Comparison of the DoA estimation on simulated and measurement data. The interference DoA is 5°. (a) DoA estimation after calibration with $\exp(-j\varphi_{\mathrm{err},n})$ shows the interference DoA as highest peak, while at 16° a high peak is generated by the falsely calibrated $S_-(f)$. (b) After a complex conjugate calibration with $\exp(+j\varphi_{\mathrm{err},n})$, $S_-(f)$ is calibrated correctly. It generates a peak at −5° according to (5). The real interference DoA is not visible anymore, but a peak at −16° is formed instead. The plots are normalized to the peak levels at +16° and −16°, respectively.

the measurement, at least 5 dB smaller than that one at 5°, so it does not contain all the energy of $S_-(f)$.

If the calibration is performed with $\exp(+j\varphi_{\mathrm{err},n})$ instead, the estimation in Fig. 12(b) shows a peak at −5° and a peak at −16°. With the complex conjugate calibration coefficients, $S_-(f)$ is calibrated correctly, this means it follows (5). The peak at −16° is generated by the falsely calibrated $S_+(f)$. The simulation behaves likewise; strong peaks occur at the same angles. The performed DoA estimations satisfy the theoretical expectations of (4)–(9).

In the next part, DBF is applied to cancel the interference DoA and amplify signals under the main direction of sight at 0°. The 8 virtual channels are processed according to (2), where the complex weights w_n follow the scheme depicted in Fig. 7 with $N = 8$. The signals of the first transmitter correspond to channels 1–4, while the signals of the second transmitter correspond to channels 5–8. This leads to the pattern in Fig. 13. It shows a notch toward the actual interference direction 5°, while a maximum appears at 0°. Although the main look direction is close to the notch at 5°, the virtual aperture is wide enough to steer a maximum there. For comparison, the similar pattern for an ideal array, i.e., without the need for any calibration, is shown. It would require notches at ±5° to cancel the interference, what is a

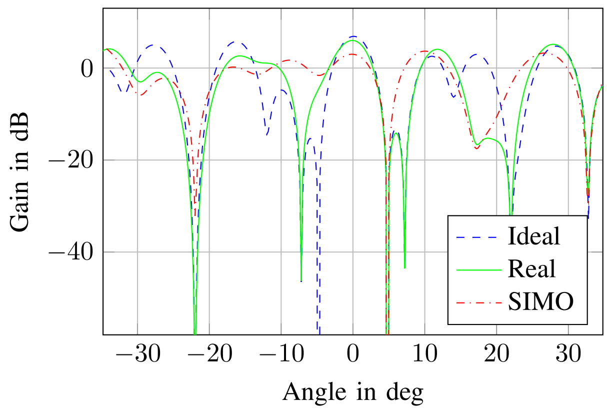

Fig. 13. Real DBF pattern including the influence of the calibration compared to the DBF pattern in an ideal array. Both patterns are designed to cancel the interference from 5° and focus the DoA 0°. The ideal array (all l_n=0 in Fig. 3) must also place a notch at −5°, as no IQ mixer is available. For comparison, the pattern of a four-element SIMO array is also shown. It has lower gain and wider peaks than the MIMO pattern.

TABLE I
COMPARISON OF THE MEASURED SNIR VALUES FOR THE SCENARIO IN FIG. 13

Target Range	DoA	Interference-free	Interfered	DBF
3.8 m	31°	9.6 dB	1 dB	13.5 dB
5 m	14°	29 dB	17.9 dB	28 dB
6 m	5°	26.8 dB	14.5 dB	17.2 dB

more severe limitation for a sensor's field of view. The figure also includes the pattern of the four-element SIMO array for the case of only one active transmitter. Compared with the MIMO pattern, it has 3 dB less gain in the 0°-direction, as only half the elements are available. It also shows much wider peaks, i.e., the curve shape is smoother. This is reasonable, because the MIMO array offers a higher resolution than the SIMO array. Targets in close neighborhood can be separated more easily through the MIMO application.

In the spectrum in Fig. 11, the interference-induced noise floor is removed by the beamformer to the largest part. The SNIR values of the targets change to 13.5 dB for the first, 28 dB for the second, and 17.2 dB for the third target. Beneath suppressing interference, the beamformer even achieves a gain for the first target compared to the interference-free situation. The SNIR values for all three cases are summarized in Table I. The target corresponding to the interference is nearly 10 dB smaller than in the interference-free case, because it is also affected by the notch at 5°. Still, the SNIR values of all targets are higher after DBF than in the case of noncoherent integration without interference suppression.

V. CONCLUSION

If an FMCW or chirp sequence radar receiver is designed without IQ mixer, a digital beamformer cannot remove interferences by just placing a notch in the beam pattern toward the interference DoAs. Half of the interference energy is also spread over other DoAs and must be taken into account as well. It depends on the particular hardware realization to which directions this energy corresponds, but this can be determined with a calibration measurement.

It was shown that in an MIMO system, a beamformer cannot make use of the virtual aperture to counteract interferences from other radars. Interference cancellation is possible only with signals of the subarrays generated by single transmitters. However, the virtual aperture can still be used to steer beams toward desired directions after interference was canceled. With knowledge of these circumstances, a beamformer can remove interfering signals and lead to significant improvements in SNIR. In the measurement shown here with a 76 GHz radar, a gain in SNIR of up to 12.5 dB could be achieved.

REFERENCES

[1] D. Oprisan and H. Rohling, "Analysis of mutual interference between automotive radar systems," in *Proc. Int. Radar Symp. (IRS)*, Berlin, Germany, 2005, pp. 83–90.
[2] G. M. Brooker, "Mutual interference of millimeter-wave radar systems," *IEEE Trans. Electromagn. Compat.*, vol. 49, no. 1, pp. 170–181, Feb. 2007.
[3] M. Goppelt, H.-L. Blöcher, and W. Menzel, "Analytical investigation of mutual interference between automotive FMCW radar sensors," in *Proc. German Microw. Conf. (GeMIC)*, Mar. 2011, pp. 1–4.
[4] X. Song, P. Willett, and S. Zhou, "Jammer detection and estimation with MIMO radar," in *Proc. Conf. Rec. 46th Asilomar Conf. Signals, Syst. Comput. (ASILOMAR)*, Nov. 2012, pp. 1312–1316.
[5] Y. Li, S. A. Vorobyov, and A. Hassanien, "Robust beamforming for jammers suppression in MIMO radar," in *Proc. IEEE Radar Conf.*, May 2014, pp. 0629–0634.
[6] C. Fischer, M. Goppelt, H.-L. Blöcher, and J. Dickmann, "Minimizing interference in automotive radar using digital beamforming," *Adv. Radio Sci.*, vol. 9, pp. 45–48, Jul. 2011. [Online]. Available: http://www.adv-radio-sci.net/9/45/2011/
[7] C. Fischer, H.-L. Blöcher, J. Dickmann, and W. Menzel, "Robust detection and mitigation of mutual interference in automotive radar," in *Proc. 16th Int. Radar Symp. (IRS)*, Jun. 2015, pp. 143–148.
[8] J. Bechter, K. Eid, F. Roos, and C. Waldschmidt, "Digital beamforming to mitigate automotive radar interference," in *IEEE MTT-S Int. Microw. Symp. Dig.*, May 2016, pp. 1–4.
[9] T. Schipper, M. Harter, T. Mahler, O. Kern, and T. Zwick, "Discussion of the operating range of frequency modulated radars in the presence of interference," *Int. J. Microw. Wireless Technol.*, vol. 6, pp. 371–378, Jun. 2014.
[10] K. Forsythe and D. Bliss, *MIMO Radar Signal Processing*, J. Li and P. Stoica, Eds. Hoboken, NJ, USA: Wiley, 2009.
[11] C. M. Schmid, R. Feger, C. Pfeffer, and A. Stelzer, "Motion compensation and efficient array design for TDMA FMCW MIMO radar systems," in *Proc. 6th Eur. Conf. Antennas Propag. (EUCAP)*, Mar. 2012, pp. 1746–1750.
[12] A. Zwanetski, M. Kronauge, and H. Rohling, "Waveform design for FMCW MIMO radar based on frequency division," in *Proc. 14th Int. Radar Symp. (IRS)*, vol. 1. Jun. 2013, pp. 89–94.
[13] R. Feger, C. Pfeffer, and A. Stelzer, "A frequency-division MIMO FMCW radar system using delta–sigma-based transmitters," in *IEEE MTT-S Int. Microw. Symp. Dig.*, Jun. 2014, pp. 1–4.
[14] R. Feger, H. Haderer, and A. Stelzer, "Optimization of codes and weighting functions for binary phase-coded FMCW MIMO radars," in *IEEE MTT-S Int. Microw. Symp. Dig.*, May 2016, pp. 1–4.
[15] D. Zoeke and A. Ziroff, "Phase migration effects in moving target localization using switched MIMO arrays," in *Proc. Eur. Radar Conf. (EuRAD)*, Sep. 2015, pp. 85–88.
[16] H. Rohling, "Radar CFAR thresholding in clutter and multiple target situations," *IEEE Trans. Aerosp. Electron. Syst.*, vol. AES-19, no. 4, pp. 608–621, Jul. 1983.
[17] S. Haykin and K. J. Ray Liu, *Handbook on Array Processing and Sensor Networks*. Hoboken, NJ, USA: Wiley, 2009. [Online]. Available: http://proquest.tech.safaribooksonline.de/9780470371763

Jonathan Bechter (GS'16) received the M.Sc. degree from Ulm University, Ulm, Germany, in 2013, where he is currently pursuing the Ph.D. degree as a Research Assistant with the Institute of Microwave Engineering.

He is involved in radar interferences and signal processing in the field of automotive radars.

Muhammad Rameez received the B.E. degree in electrical engineering from the National University of Sciences and Technology, Islamabad, Pakistan, in 2010, and the M.Sc. degree in communications technology from the University of Ulm, Ulm, Germany, in 2016. He is currently pursuing the Ph.D. degree in systems engineering at the Blekinge Insitute of Technology, Karlshamn, Sweden.

His current research interests include algorithm development for target detection and tracking in traffic monitoring radars.

Christian Waldschmidt (M'13–SM'13) received the Dipl.-Ing. (M.S.E.E.) and Dr.-Ing. (Ph.D.E.E.) degrees from the Universität Karlsruhe (TH), Karlsruhe, Germany, in 2001 and 2004, respectively.

From 2001 to 2004, he was a Research Assistant with the Institut fãr Hãchstfrequenztechnik and Elektronik, TH. He was heading different research and development teams in microwave engineering, RF-sensing, and automotive radar. In 2013, he returned to academia. He then became the Director with the Institute of Microwave Engineering, Ulm University, Ulm, Germany, where he was a Full Professor. His researches focus on radar and RF-sensing, millimeter-wave, and submillimeter-wave engineering, antennas and antenna arrays, RF, and array signal processing. Since 2004, he has been with the business units Corporate Research and Chassis Systems with Robert Bosch GmbH, Stuttgart, Germany. He has authored or co-authored over 100 scientific publications and holds 20 patents.

Mr. Waldschmidt is the Vice Chair of the IEEE MTT-27 Technical Committee (Wireless Enabled Automotive and Vehicular Applications), an Executive Committee Board Member of the German MTT/AP Joint Chapter, and a member of the ITG Committee Microwave Engineering. In 2015, he served as the TPC Chair of the IEEE Microwave Theory and Techniques Society International Conference on Microwaves for Intelligent Mobility. He is a reviewer for multiple IEEE TRANSACTIONS and LETTERS.